

Carbamohydrazonothioate derivative—experimental and theoretical explorations of the crystal and molecular structure

Barbara Bankiewicz¹ · Sławomir Wojtulewski¹ · Karolina H. Markiewicz^{1,2} · Agnieszka Z. Wilczewska^{1,2}

Received: 29 July 2016 / Accepted: 4 November 2016 / Published online: 28 November 2016
© The Author(s) 2016. This article is published with open access at Springerlink.com

Abstract The structural studies of carbamohydrazonothioate derivative and its hydrochloride solvate are the aim of hereunder presented research. The combination of the crystallographic techniques and the Hirshfeld surface analysis allows to describe the net of the hydrogen bonds as well as other non-covalent interactions within the crystal structures. The crystal structures of 4-ethenylbenzyl N'-[(E)-phenylmethylidene] carbamohydrazonothioate (CHT) and CHT hydrochloride solvate are built of bent and linear conformers of the carbamohydrazonothioate derivative, respectively. The theoretical calculations indicate that the alteration of the conformation is possible. While the geometry of the bent conformers allows the crystal structure to propagate, the linear conformation does not encourage formation of the intermolecular interactions between CHT molecules. Therefore, in the latter case, the chloride ions and methanol play the role of the molecular glue. In both crystal structures, the dominant is H···H interaction; thus, the dispersion energy is an important factor in intermolecular interactions. The theoretical calculations for single molecules and dimers of CHT show the negligible influence of the crystal packing on molecular conformation and dimer formation, when the dispersion energy correction is applied.

Keywords Carbamohydrazonothioate · Crystal structure · Hirshfeld surface · DFT · Dispersion energy

Introduction

Thiosemicarbazone derivatives represent a group of organic compounds that have been intensively explored because of the broad spectrum of their biological activities [1–3]. It is also one of the several classes of chelating ligands for transition metal ions. Thiosemicarbazones possess two possible complexing centres, the sulphur atom and azomethine nitrogen atom. They combine mixed hard-soft donor character and versatile coordination ability [4, 5], which are determined by the structure of a particular compound. Numerous metal complexes of various thiosemicarbazones have been investigated [4–14]. A significant attention has been drawn to their medicinal applications. They are commonly used in the treatment of many diseases [15–18] because of their biological properties (i.e. antibacterial, antiviral and antineoplastic activity) and the ability to diffuse through the semipermeable cell membranes [5, 19–22]. Furthermore, some metal complexes of thiosemicarbazones were reported to have analytical applications for metal ion determination, extraction and removal [23–26].

A wide range of application in many different scientific fields is the reason why new chelating ligands, based on thiosemicarbazones structure, are still designed. Usually, the main chelating molecular fragment is modified by addition of terminal functional groups. For example, ligand molecule enriched with a vinyl group can be used as a monomer in a radical polymerization reaction [21, 27–29].

In this paper, we present the full structural characterization and theoretical studies of new ligand based on thiosemicarbazide structure, namely 4-ethenylbenzyl N'-[(E)-phenylmethylidene] carbamohydrazonothioate (CHT).

Electronic supplementary material The online version of this article (doi:10.1007/s11224-016-0874-y) contains supplementary material, which is available to authorized users.

✉ Sławomir Wojtulewski
s.wojtulewski@uwb.edu.pl

¹ Institute of Chemistry, University of Białystok, Ciołkowskiego 1K, 15-245 Białystok, Poland

² Laboratory of New Technologies of Synthesis and Analysis of Polymers, Center of Synthesis and Analysis BioNanoTechno of University of Białystok, Ciołkowskiego 1K, 15-245 Białystok, Poland

Experimental section

The synthesis of 4-ethenylbenzyl N'-[(E)-phenylmethylidene] carbamohydrazonothioate and its hydrochloride solvate is described elsewhere [27]. To obtain crystals appropriate for X-ray measurements, a series of the crystallization experiments with various solvents were performed. The crystals of the CHT and its solvated hydrochloride form (CHT-salt) were grown by slow evaporation from methanol solution.

Crystallographic data

The X-ray data were collected on an Oxford Diffraction SuperNova DualSource diffractometer with a monochromated Mo K α X-ray source at 100K. Data reduction and multi-scan absorption correction were performed with CrysAlis PRO [30]. The crystal structures were solved and refined using Olex2 combined with SHELXS and SHELXL97 programs [31–33]. All hydrogen atoms were located in electron density difference maps. The non-hydrogen atoms were refined anisotropically.

The summary of relevant crystallographic data for both CHT and CHT-salt is given in Table 1. The CCDC-1049864 (CHT) and CCDC-1049967 (CHT-salt) contain the supplementary crystallographic data for this paper. These data can be obtained free of charge from the Cambridge Crystallographic Data Centre via www.ccdc.cam.ac.uk/data_request/cif.

Hirshfeld surface calculation

Based on the refined and deposited crystal structures, the Hirshfeld surface for CHT and CHT-salt was generated using CrystalExplorer 3.1 program [34]. In order to determine the kinds of non-covalent interactions in the crystal structures, the normalized contact distances, d_{norm} [35], were mapped into the Hirshfeld surfaces. The three types of contact in relation to the van der Waals radii are in question here. Shorter than the sum of the van der Waals (VdW) radii (d_{norm} negative), close to the sum of the VdW radii (d_{norm} equal zero) and longer than the sum of the VdW radii (d_{norm} positive) are colored red, white and blue, respectively. Additionally, the Hirshfeld surface fingerprint plots were generated. They are 2D histograms of the d_i and d_e

Table 1 Crystal data and structure refinement for CHT and CHT-salt

	CHT	CHT-salt
Empirical formula	C ₁₇ H ₁₇ N ₃ S	C ₁₇ H ₁₈ N ₃ S ¹⁺ , C ₁ H ₄ O ₁ , Cl ¹⁻
Formula weight, g/mol	295.41	363.90
Crystal size/mm ³	0.484 × 0.422 × 0.040	0.298 × 0.213 × 0.093
Crystal system	triclinic	triclinic
Space group	$P\bar{1}$	$P\bar{1}$
a/Å	8.665 (7)	9.417 (6)
b/Å	9.386 (5)	10.225 (6)
c/Å	10.489 (7)	11.86 (4)
$\alpha/^\circ$	84.169 (2)	67.799 (2)
$\beta/^\circ$	87.261 (12)	68.787 (2)
$\gamma/^\circ$	64.997 (2)	66.310 (2)
Volume/Å ³	769.26 (4)	938.49 (4)
Z	2	2
$\rho_{\text{calc}}/\text{cm}^3$	1.2753	1.288
μ/mm	0.207	0.324
Temperature/K	100	100
Radiation	Mo K α (λ = 0.71073)	Mo K α (λ = 0.71073)
Completeness (%)	99.7	99.9
2 θ range/ $^\circ$	5.92 to 72.62	5.54 to 72.64
Reflections collected	37,171	45,409
Independent reflections	7441 [R_{int} = 0.0412, R_{sigma} = 0.0269]	9081 [R_{int} = 0.0463, R_{sigma} = 0.0338]
Parameters /restraints	205/0	230/0
Goodness-of-fit on F ²	1.098	1.034
Final R indexes [$I \geq 2\sigma(I)$]	R_1 = 0.0404, wR_2 = 0.1062	R_1 = 0.0446, wR_2 = 0.1116
Final R indexes [all data]	R_1 = 0.0519, wR_2 = 0.1179	R_1 = 0.0656, wR_2 = 0.1258
Largest diff. peak/hole/e/Å ³	0.66/−0.30	0.72/−0.34

distances. The d_i corresponds to the distance from the surface to the nearest atom in the molecule itself, whereas the d_e corresponds to the distance from the surface to the nearest atom of the neighbor molecule. The proportional contribution of the contact pairs in the global surface is described with a color gradient in the plots going from blue to red.

Computational details

To gain quantitative insight into relevant structural and energy parameters, monomers and dimers of the two conformations of CHT ligand were optimized computationally. The calculations were performed under gas phase conditions using the DFT-B3LYP [36–39] method implemented in Gaussian 09 [40] program. Functional was used in conjunction with the 6–311++G(d,p) [41] basis set. Additionally, it was combined with the Grimme's D2 dispersion correction [42]. The B3LYP functional was chosen since it was reported in several benchmark studies that this functional reproduces geometry parameters very well [43] and in general is recommended as the functional achieving acceptable accuracy for a very large group of molecular systems of various characteristics [44–46]. Geometries of all the systems were extracted from the crystal structure and optimized without any symmetry constraints.

In order to verify if the optimized geometries correspond to stationary points, the frequency analysis at the same level of theory was performed. It should be noted that full optimization failed for the N–H \cdots N-type dimer. Imaginary frequencies were observed for dimer modeled using two levels of theory, B3LYP/311++G(d,p) and B3LYP/311++G(d,p), with Grimme's D2 correction, and they amounted respectively $-2.81/\text{cm}$ and $-3.36/\text{cm}$. The occurrence of imaginary frequencies is related to the accuracy of a numerical integration model in the calculation method. Systems with very low imaginary frequencies (*close-to-zero frequencies*) are close to stationary points, and they are situated near the minimum on the surface of the potential energy [47]. Because of this sometimes, systems with imaginary frequency row $-20/\text{cm}$ are analyzed, considering it as a representative and equivalent to the stationary points. To preserve the coherence of the analyses referred, molecular models have been taken into account in research. In other cases, no imaginary frequencies were found. Received equilibrium systems fulfil the criteria for convergence and they correspond to the local energy minima.

The total interaction energy in the optimized dimers was calculated in the supermolecular fashion. The sum of the total energies of isolated molecules of CHT ligand in their geometries found in dimer was subtracted from the total energy of these dimers. To remove the basis set superposition error (BSSE) from the values of dimer interaction energies, the counterpoise correction method of Boys and Bernardi [48] was employed.

Additionally, the molecular electrostatic potential (MEP) was computed and mapped on the electron density isosurface of 0.0004 a.u. Plots have been obtained by means of GaussView program. Check files used for electron potential mapping were generated by Gaussian 09. To support our final conclusions, the theoretical calculations based on the quantum theory of atoms in molecules (QTAIM) [49, 50] were performed using AIMALL [51] software. Analysis of the electron density topology concerns only single molecules of bent and linear conformations of CHT ligand. Selected topological parameters including electron densities, ρ_{BCP} , and Laplacian operators, $\nabla^2 \rho_{\text{BCP}}$ at the bond critical points, BCPs, and distribution of atomic charges were obtained and studied.

Results and discussion

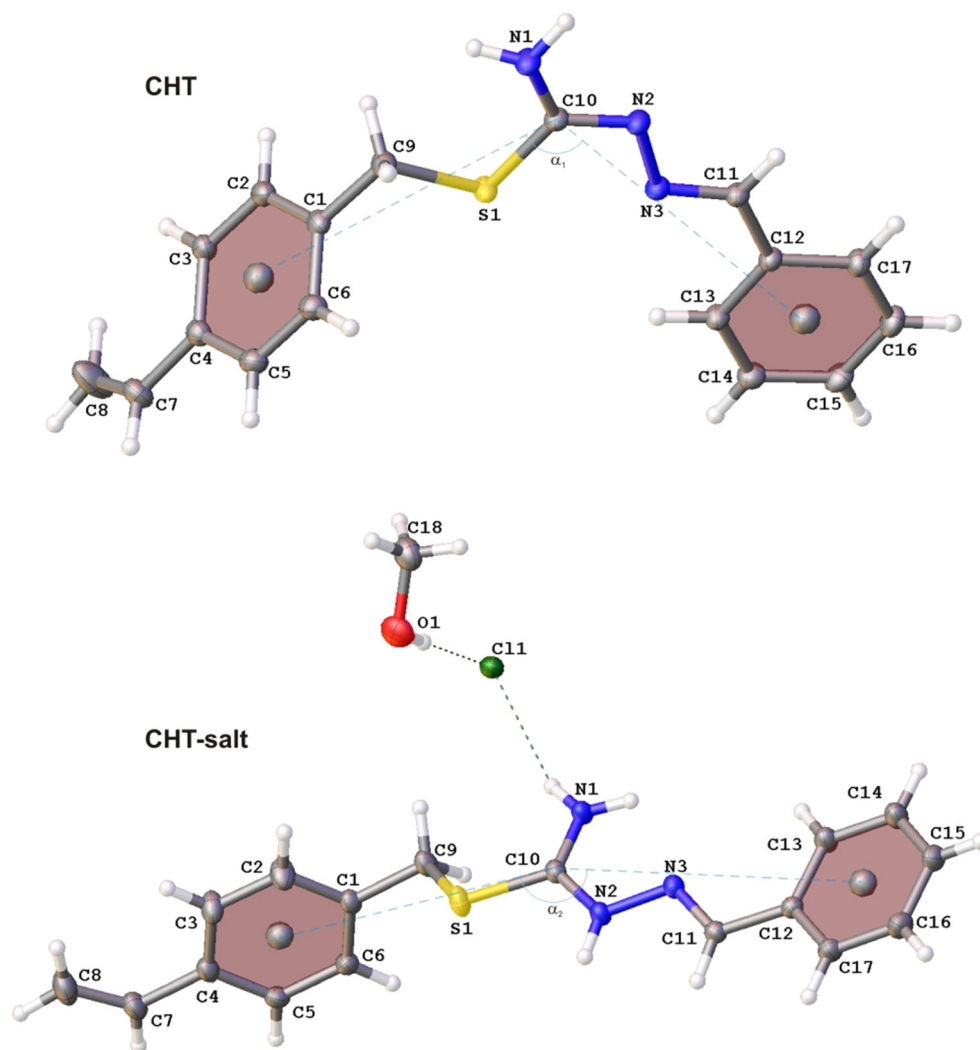
Crystal structures

The crystals of CHT and CHT-salt were obtained from methanol solutions by slow evaporation at room temperature. The crystal structure analysis reveals that the CHT is the pure form of a compound. The second structure is the solvated hydrochloride with methanol molecules.

Figure 1 depicts the asymmetric units of both crystal structures. The blue-dashed lines describe an angle between two centroids of the aromatic rings and C10 atom. The angle for CHT and CHT-salt is equal $\alpha_1 = 101.826^\circ$ and $\alpha_2 = 166.092^\circ$, respectively. Therefore, the former conformation will be designed as the bent one and the latter as the linear one. The single molecule of the ligand contains two aromatic rings. The angle between the planes of two aromatic rings is equal 73.92° for the CHT and 80.67° for the CHT-salt. Thus, one can clearly see that the main difference between these two structures is their conformation.

Figure 2 depicts the mutual orientation of molecules in the crystal structures. The two CHT molecules form two types of dimers. The molecules are linked by cyclic hydrogen bonds N–H \cdots N type, where N1–H1A bond of the amino group is the donor and an N2 atom of the neighbor molecule is the acceptor. This is the main motif of this structure. The PLATON report notes the absence of a hydrogen bond acceptor for N1–H1B. However, the detailed study shows that the amino group forms only one non-covalent interaction in this crystal structure. Due to the nearly perpendicular orientation of the aromatic rings within one molecule, the second type of dimer is formed through the cyclic hydrogen bonds C–H $\cdots\pi$ type. The net of alternately arranged two types of dimers creates an infinite ribbon of molecules (Fig. 2), and the parallel ribbons create sheets. The distance between neighboring sheets is 3.360 Å. They are also offset by 7.990 Å (Fig. S1 in Online Resources). The essential geometrical parameters of the hydrogen bonds (HBs) are presented in Table S3 (Online Resources).

Fig. 1 The asymmetric units of crystal structures of the CHT and CHT-salt

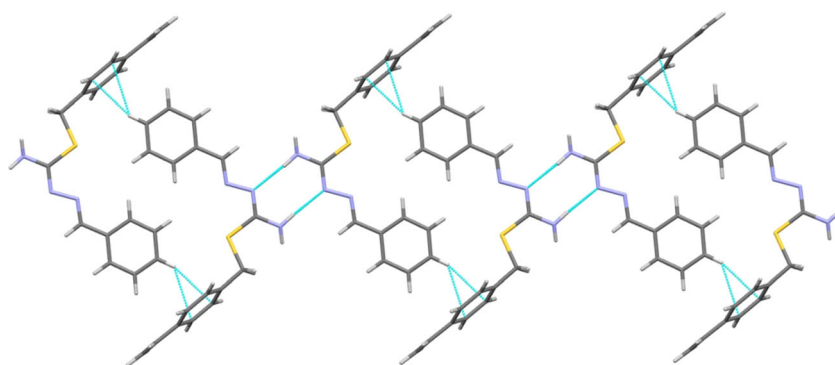


The CHT-salt crystal structure is more complicated. It is impossible to distinguish main motif here. The situation is clearer when the net of the HBs and other contacts is separated.

The chloride anions play a dominant role in the crystal structure of the CHT-salt. Together with the methanol molecules, they bind the stacks of the cation molecules. The methanol molecule and chloride ion play the role of the molecular glue for the crystal structure (Fig. 3a).

The hydrochloride's proton covalently bonded to the nitrogen atom (N2) forms the cation molecule. The molecules are linked through the net of charge-assisted hydrogen bonds CAHBs built of chloride anion and methanol molecule. There are three types of CAHBs here: $\text{N-H}\cdots\text{Cl}(-)$, $\text{O-H}\cdots\text{Cl}(-)$ and $(+)\text{N-H}\cdots\text{O}$ (Table S3 in Online Resources). In the case of the first two CAHBs, the chloride anion is the acceptor, while the amino group of the cation and the hydroxyl group of the methanol

Fig. 2 The ribbon of molecules generated in the crystal structure



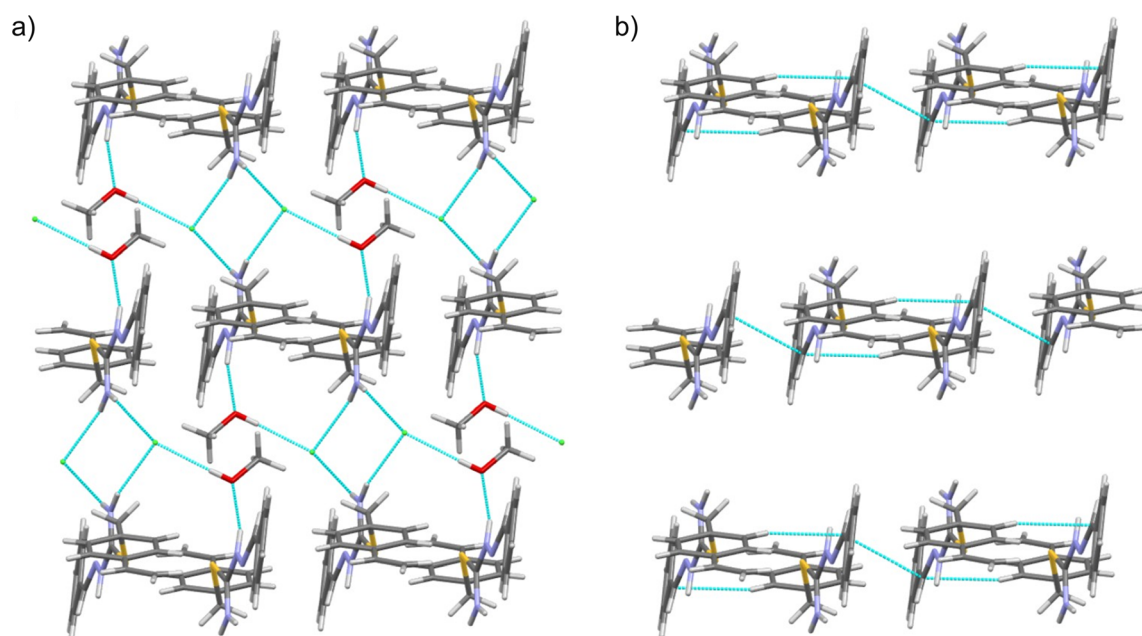


Fig. 3 The net of the **a** hydrogen bonds and **b** intermolecular interactions of the CHT-salt crystal structure. The chloride anions and methanol molecules were omitted on **b** for the clarity

molecule are donors. The hydroxyl group of the methanol molecule is also the HB acceptor in the case of the third CAHB, where (+)N2–H bond acts as a donor (Fig. 3a). Figure 3b shows the same fragment of the crystal structure, but chloride anions and methanol molecules were not included. Blue-dashed lines represent the intermolecular contacts shorter than the sum of the VdW radii. They are described as short contacts by standard settings of the Mercury program. Two molecules of the cation are arranged anti-parallel and placed one over another forming the C–H \cdots C contacts. There is also C \cdots C-type contact between another pair of the ligand cations; however, further analysis do not confirm that it is $\pi\cdots\pi$ interaction. The geometrical parameters of described contacts are presented in Table S3 (Online Resources).

Additional two perpendicular views of the crystal structure are presented in Figs. S2 and S3 (Online Resources). The first one highlights the net of the charge-assisted HBs. The second

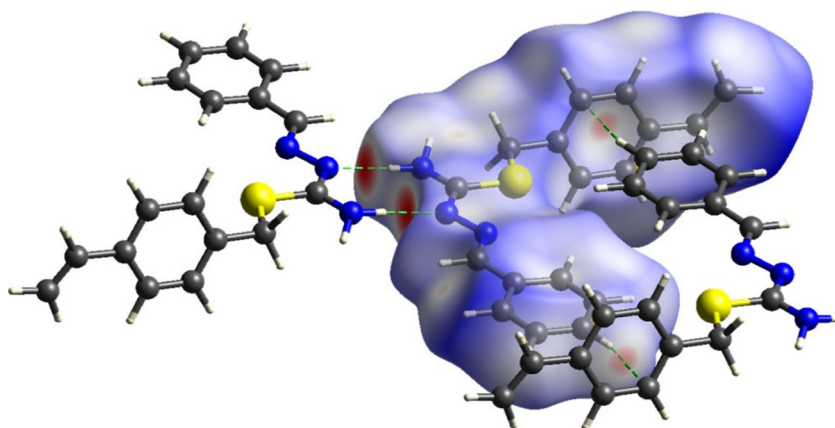
shows the intermolecular contacts shorter than the sum of the VdW radii. Despite the fact that both molecules contain aromatic rings, no $\pi\cdots\pi$ interactions were observed in the CHT or CHT-salt crystal structures.

Non-covalent interactions in crystal structures—Hirshfeld surface analysis

The above presented analysis is focused on the general arrangement of the crystal structures. The further study is based on the Hirshfeld surface (HS) analysis. It provides crucial information about the quantity and quality of non-covalent interactions in both crystal structures. The graphical presentation of HS generated for the asymmetric unit of the CHT structure is shown in Fig. 4.

Previously described cyclic HBs N–H \cdots N type are marked as two red spots on the HS, nearby hydrazoneformamide molecular fragment. Moreover, two other reddish spots are

Fig. 4 The graphical presentation of the Hirshfeld surface for the single molecule of CHT crystal structure



observed. One is located close to H15 atom of the phenol ring and the other one close to the ethenylbenzene ring. Both represent the second cyclic HBs $C-H\cdots\pi$ type. The C15–H15 bond is the donor and the π electrons of the ethenylbenzene ring are acceptor. Additionally, there are many white regions on the surface. They indicate the major interactions in the crystal structure, which are about the sum of the VdW radii.

The decomposition of the fingerprint plot (Fig. 5) shows that there are four dominant types of the intermolecular contacts: $C\cdots H$, $H\cdots H$, $N\cdots H$ and $S\cdots H$. They cover 97.4% of all non-covalent contacts in the crystal structure. The $N\cdots H$ contacts are well defined as the HBs $N-H\cdots N$ type. The H14 aromatic hydrogen atom is involved in $S\cdots H$ contacts. They are a result of packing, and their length range is about 3–5 Å. In the case of $C\cdots H$ contacts, the hydrogen atoms and the carbon atoms are aromatic and the interactions are the

consequence of the mutual position of the two aromatic rings within the single molecule. The planes of the aromatic rings are nearly perpendicular (73.92°). Furthermore, because of the bent conformation, the two molecules of the ligand match each other like the jigsaw puzzle pieces. Hence, the dimer with cyclic HBs $C-H\cdots\pi$ type is formed. The $H\cdots H$ contacts are dominant, and the shortest is between H17 and H8 of an ethylene group ($D = 2.277$ Å) as a result of packing.

As mentioned above, the CHT-salt crystal structure is more complicated. To identify intermolecular interactions for CHT-salt crystal structure, the HSs were generated for methanol molecule, chloride anion and main compound molecule cation independently. It allows to describe the contribution of each of these three fragments to the intermolecular interaction net within the crystal structure. All the red spots on the HS of the cation molecule (Fig. 6a) correspond to the intermolecular HBs. In all cases,

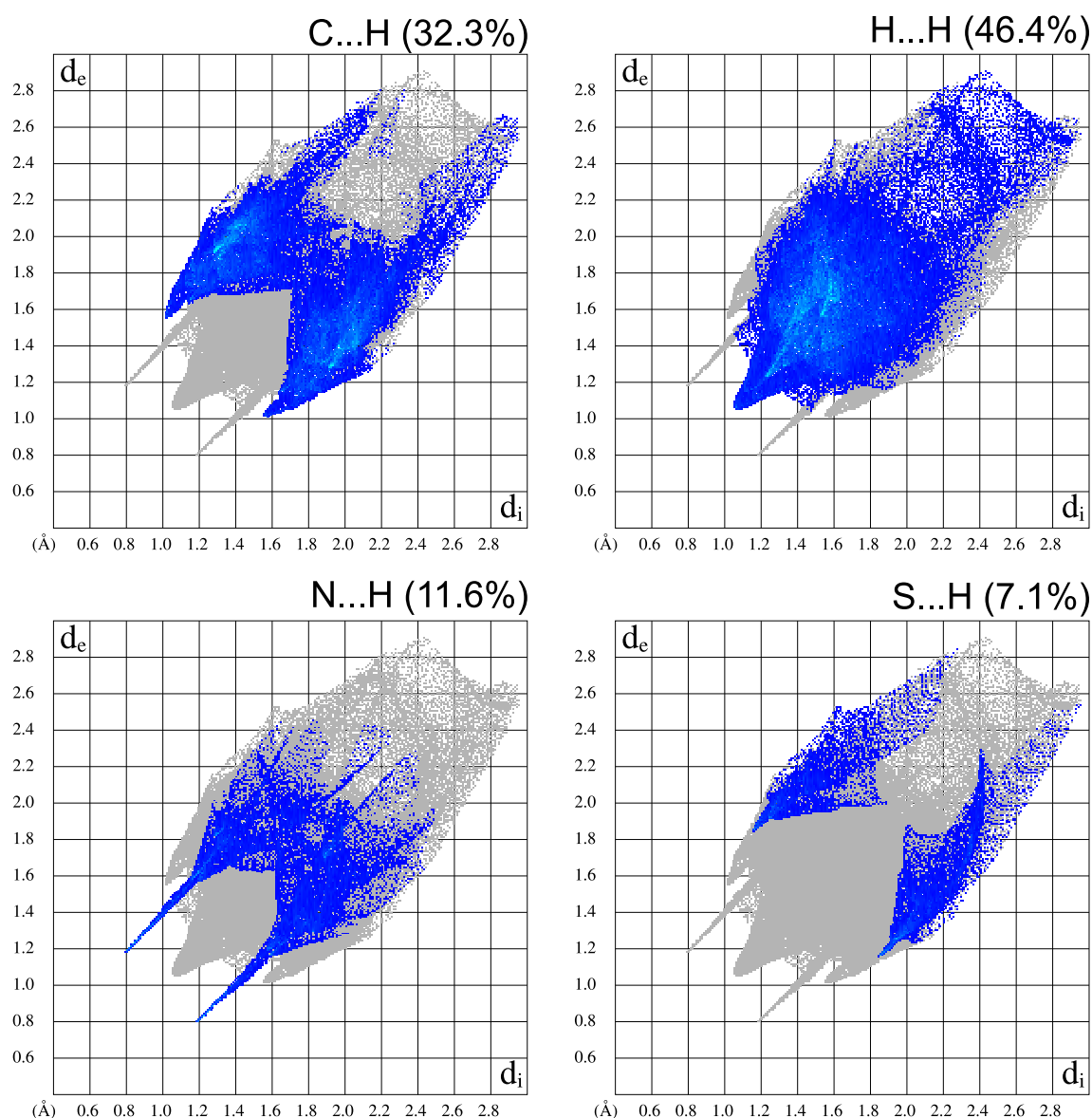


Fig. 5 The fingerprint plots with decomposition of dominant types of the intermolecular contacts of CHT crystal structure

cation molecule plays the role of a hydrogen atom donor. Namely, it is a donor for three HBs formed with chloride anions as acceptors, $\text{N1-HA}\cdots\text{Cl2}$, $\text{N1-HB}\cdots\text{Cl1}$ and $\text{C9-H9}\cdots\text{Cl2}$, and a donor for one HB with methanol molecule as the acceptor $\text{N2-HA}\cdots\text{O1}$. It is worth mentioning that the $\text{C9-H9}\cdots\text{Cl2}$ contact was displayed as a hydrogen bond by the CrystalExplorer3.1 program as a green-dashed line without changes in default settings. The distance $d_{\text{C}\cdots\text{Cl}}$ is equal to 3.597 Å. This contact is also depicted as a red spot on the HS of ligand and chloride anion as well. The chloride anion is surrounded by hydrogen atoms. Moreover, one of the HBs is an $\text{O-H}\cdots\text{Cl}$ type where the hydroxyl group of the methanol molecule is a HB's donor (Fig. 6c). The oxygen atom of the hydroxyl group is also an acceptor of the HB where the N2-H bond of the next molecule is a donor.

Decomposition of the fingerprint plot for a cation molecule shows that $\text{H}\cdots\text{H}$ and $\text{C}\cdots\text{H}$ contacts are dominant, similar to CHT crystal structure. The $\text{N}\cdots\text{H}$ and $\text{S}\cdots\text{H}$ contacts are close to or longer than the sum of the VdW radii. Furthermore, the $\text{Cl}\cdots\text{H}$ and $\text{O}\cdots\text{H}$ contacts are observed, which are HBs in nature. All six types of intermolecular contacts in question represent about 90% of all non-covalent interactions of the cation (Fig. 7a). Missing 10% are contacts longer than the sum of the VdW radii, e.g. $\text{C}\cdots\text{N}$ 2.5%, $\text{S}\cdots\text{O}$ 2.3% or $\text{S}\cdots\text{S}$ 0.5% type. They are caused by presence of charge-assisted HBs which boost close packing of the crystal structure.

Decomposed fingerprint plots for a methanol molecule revealed that the dominant intermolecular contacts are $\text{H}\cdots\text{H}$. Together with $\text{C}\cdots\text{H}$, $\text{Cl}\cdots\text{H}$ and $\text{O}\cdots\text{H}$ contacts, they cover 99.8% of all intermolecular contacts. As was aforementioned, $\text{Cl}\cdots\text{H}$ and $\text{O}\cdots\text{H}$ contacts are HBs. The $\text{H}\cdots\text{H}$ contacts are longer than the sum of the VdW radii and involve the hydrogen atoms of the methanol's methyl group (Fig. 7b).

The fingerprint plot analysis of the chloride anion shows that $\text{Cl}\cdots\text{H}$ is the only type of the intermolecular contacts. All of them are HBs in nature, and they are charge-assisted ones (Fig. 7c).

Dimerization process for CHT molecules

The analysis of the HS proves that there are two types of dimers in crystal structure of CHT. One is formed through the $\text{N-H}\cdots\text{N}$ cyclic HBs, and second is formed through the $\text{C-H}\cdots\pi$ cyclic HBs (Fig. 2). To estimate the energy of both non-covalent interactions, the calculations for isolated dimers were performed on the B3LYP/6-311++G(d,p) level of theory. The analysis based on the Hirshfeld surface of the ligand molecule leads to the observation that the dominant interactions in the crystal structure are $\text{H}\cdots\text{H}$ and $\text{C}\cdots\text{H}$ types. These interactions are weak and the dispersion is a significant factor here. Since the set of density functional theory (DFT) functionals applied here does not take into account the dispersion interaction energy, the second set of optimizations with the use of Grimme GD2 empirical dispersion correction was done. This procedure allows to measure how the dispersion energy influences each type of interaction. The geometries of the optimized dimers were compared with the adequate molecular fragments of crystal structure. The overlays include only non-hydrogen atoms and are depicted in Fig. 8a and 8a'. In the case of $\text{N-H}\cdots\text{N}$ type dimer, no significant differences are observed. The root-mean-square deviation (RMSD) and maximum distance (Max. D) values are essentially equal regardless of the GD2 dispersion correction application. Surprisingly, good reproduction of the dimer shows marginal influence of the crystal packing on the $\text{N-H}\cdots\text{N}$ dimer formation. Both approximations, with and without GD2 dispersion correction, reproduce the general shape of the $\text{C-H}\cdots\pi$ dimer (Fig. 8b and 8b'). It proves that the influence of the crystal packing is negligible in

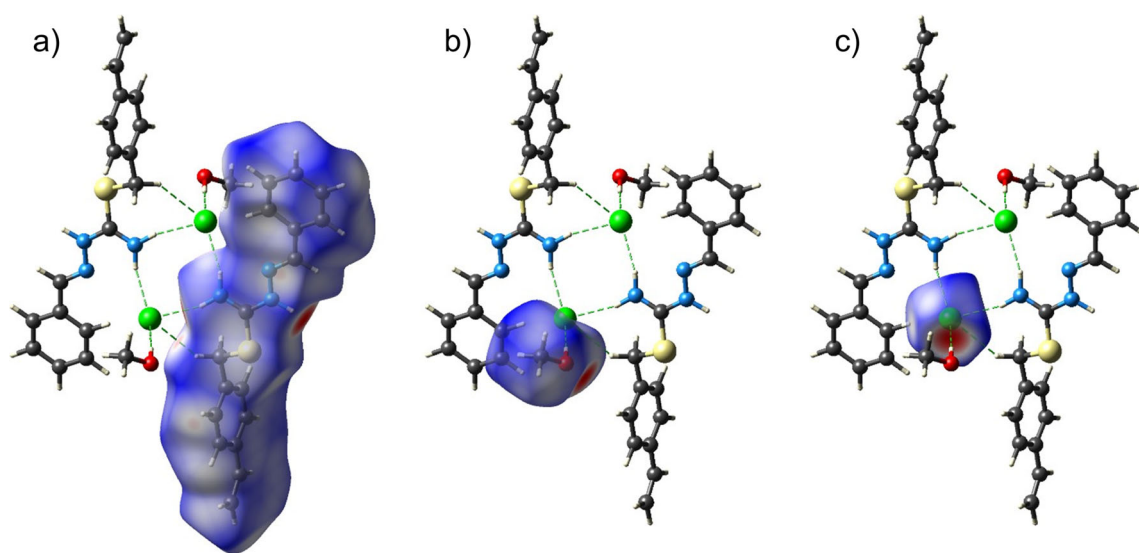


Fig. 6 The graphical presentation of the Hirshfeld surface for fragments of the CHT-salt crystal structure. **a** Cation molecule. **b** Chloride anion. **c** Methanol molecule

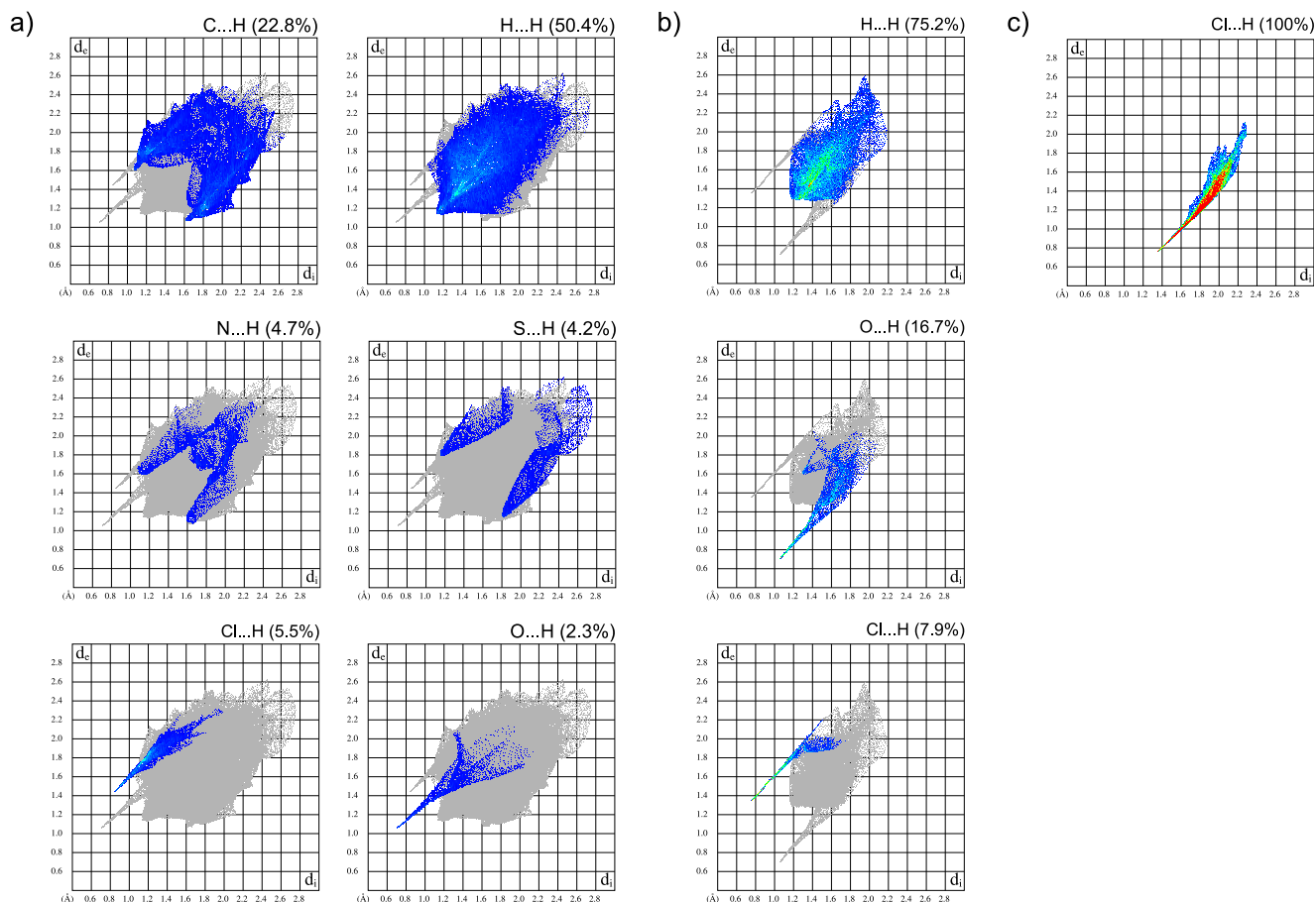


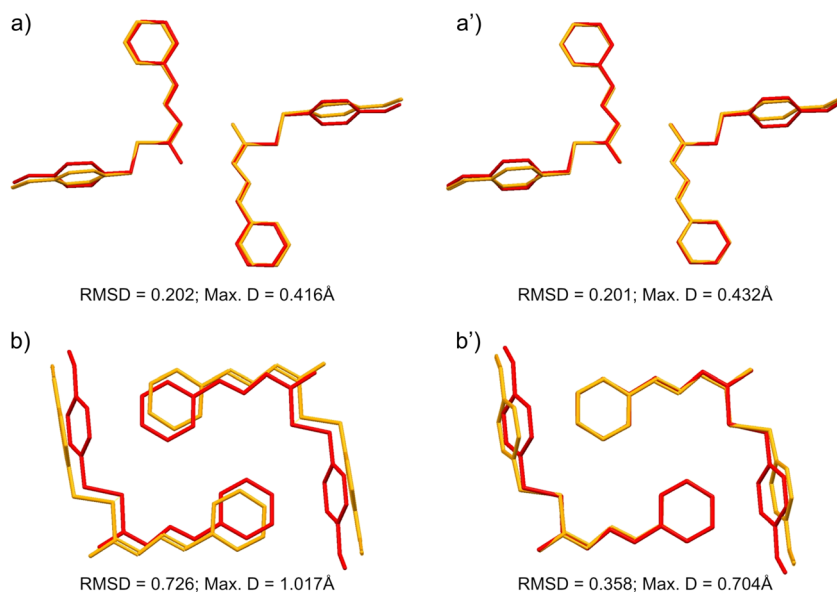
Fig. 7 The fingerprint plots with decomposition of dominant types of the intermolecular contacts. **a** Cation molecule. **b** Methanol molecule. **c** Chloride anion

the case of the second type of the studied dimer also. Nevertheless, the results of the calculations, which include dispersion energy, give better overlay of the structural fragments.

The N–H bond and an N atom are described by Desiraju and Steiner [52] as a strong donor and a strong acceptor, respectively.

The same authors defined the C–H bond as a weak donor and aromatic electrons as a weak acceptor. In the cases of heteronuclear dimer HBs, such as N–H...O and O–H...N, calculated (at an MP2/6–311++G(d,p) level of theory) energy values are about –50 kJ (–12 kcal/mol) and –84 kJ (–20 kcal/mol),

Fig. 8 Structure overlay of two type dimers. Red indicates real X-ray structures; orange indicates theoretical models. **a**, **b** B3LYP/6–311++G(d,p). **a'**, **b'** B3LYP/6–311++G(d,p) with GD2 empirical dispersion correction



respectively [53]. The calculations for C–H $\cdots\pi$ hydrogen bonds show that they are not stronger than 4 kJ (1 kcal/mol) [54].

The dimerization energy was calculated as a difference between the dimer energy and the single molecule energies. The energies and BSSE values were collected in Table S4 (Online Resources). The energy values obtained from DFT calculations, where the dispersion correction was not applied, show that the homonuclear N–H \cdots N dimerization energy equals to –49.32 kJ (–11.78 kcal/mol), while in the case of the C–H $\cdots\pi$ type, dimerization energy is close to zero. The application of the dispersion correction increases the dimerization energy up to –73.10 kJ (–17.46 kcal/mol) for N–H \cdots N system. For C–H $\cdots\pi$, dimer energy is equal to –49.15 kJ (–11.74 kcal/mol) and is overestimated.

The chosen calculation method gives only raw estimation of the non-covalent interaction energy. Nevertheless, the combination of the B3LYP/6–311++G(d,p) level of theory with GD2 dispersion correction provides correct geometries of the studied dimers.

Rotation process

Because of the main conformational difference between molecules in both crystal structures, it is possible to go from one conformation to another. The process can be arranged by rotation defined as an alternation of the dihedral angle N1C10N2N3. The angle in the crystal structures is equal to 175.99° and 11.72° for CHT and CHT-salt systems, respectively. To prove our supposition, the optimization calculations for the bent and the linear conformations of the isolated CHT molecule were performed. The optimization process led to the potential energy surface local minima and no imaginary frequencies were found.

The calculated geometries of the bent and the linear conformations were compared with the ligand molecules of appropriate crystal structures. The structural overlay concerns only non-hydrogen atoms. The comparisons are depicted in Fig. 9. The a and a' overlays concern the CHT structure conformations calculated without and with dispersion correction GD2,

respectively. The comparison for the linear conformation (Fig. 9b and b') was performed in the same manner. This time, the reference molecule was a cation of the CHT-salt structure. Regardless of the used dispersion correction, the RMSD changes slightly in all cases. Its value is lower when the B3LYP set of functionals is combined with 6/311++G(d,p) basis set and GD2 Grimme empirical correction. Similarly to the situation described in the case of dimers, the packing effect of the crystal structure does not have an influence on the conformations of the molecules. Moreover, the cation of the CHT-salt crystal structure was compared with an optimized neutral molecule. It appeared that protonation does not influence the conformation as well.

Table 2 contains the values of the dihedral angle N1C1N2N3 for two conformations and transition state (TS) optimized on the different levels of theory. Additionally, data set covers the energy of the conformers and the energy of the rotation barrier (TS) in relation to the bent conformation. The TS geometry was proven by the one imaginary frequency. Moreover, the intrinsic reaction coordinate (IRC) calculations were performed. Two local minima are connected through the TS, which confirms the existence of the reaction path for rotation process. The energetic diagram (Fig. S4 in Online Resources) shows the results of the IRC calculations. It is worth mentioning that in the IRC calculations, all geometrical parameters are considered as variables thus are free to change when the reaction path is followed. The bent and the linear conformations are energetically equivalent and the rotation barrier is around 96 kJ (23 kcal/mol). This proves that the change of the conformation is possible and there is no steric hindrance during the process. Nevertheless, the rotation barrier is quite high and the change of the conformation might not be spontaneous.

Electrostatic potential surface and charge distribution

The molecules of the bent conformation easily form dimers in contrast to the molecules of the linear conformation. To explain these phenomena, the electrostatic potential surface was

Fig. 9 The overlay of the molecules for two conformations **a** bent and **b** linear. The geometries of the crystal structures are colored *red*. The calculated geometries are colored *orange*. The hydrogen atoms were omitted for clarity

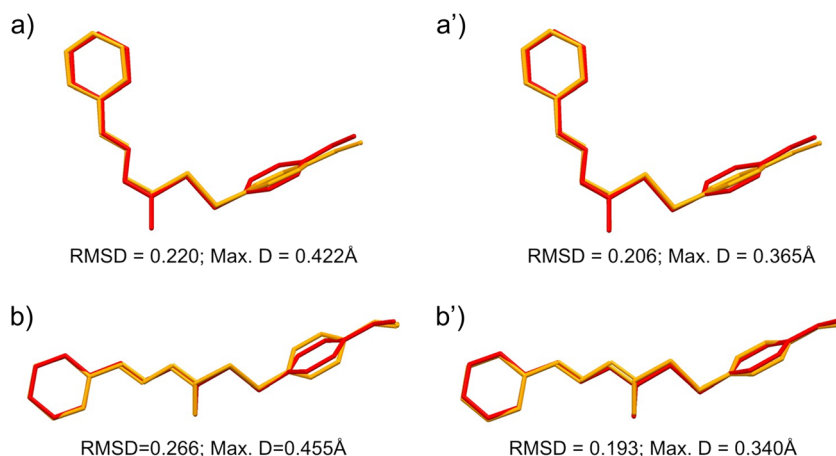


Table 2 The values of the energy [kJ] ([kcal/mol]) of the optimized conformations in relation to the bent conformation and the values of the dihedral angle N1C10N2N3 [°]

Level of theory	Bent	TS	Linear
B3LYP/6-311++G(d,p)	0.000	174.8	95.823 (22.887)
B3LYP/6-311++G(d,p) GD2	0.000	175.1	96.937 (23.153)

calculated. The electrostatic potential was mapped on the 0.0004 a.u. molecular isosurface of the electron density. The colored scale corresponds to values in range -0.07 to $+0.07$ Hartree for red and blue, respectively.

The analyses of molecular electrostatic potential of both conformers show that the negative charge is collected on phenyl ring and nitrogen atoms in N=N bond of hydrazoneformamide fragment, whereas the positive regions of molecules are found in vicinity of hydrogen atoms of an amino group and phenyl rings. When comparing the hydrazoneformamide fragment of the bent and linear conformations, the shift of the electrostatic potential can be observed. Due to rotation, the negative electrostatic potential located between an amino group and a hydrogen atom of C11 (bent conformation) moves to the opposite part of the molecule (linear conformation). Figure 10 depicts the shift of the red-colored region close to the N–N bond in relation to the conformational alteration.

In the case of the bent form of the ligand, proximity of negative charge collected on the nitrogen atoms in N–N bond and positive charge on the hydrogens of the amino group

allows to form a cyclic hydrogen bond between two molecules. The linear conformation separates these two regions. Moreover, formation of the strong non-covalent intermolecular interaction is not easy because of a steric hindrance.

To estimate quantitative changes of the atomic charges, the electronic charge distribution in terms of the QTAIM was calculated. The values of integrated charges for atomic basins are consistent with the electrostatic potential energy maps. Table S6 (Online Resources) contains the changes in the charge distribution between bent and linear conformations. The detailed analysis of the atomic charge distribution presented in Table S6 (Online Resources) shows that the change of conformation does not influence the atomic charge population in general. The exception is hydrazoneformamide fragment. The electronic charges are shifted from N1H1A and C11N3 covalent bonds to the N1 and N3 nitrogen atoms, respectively. Hence, the negative atomic charges of N1 and N3 increase as well as the positive charge on the hydrogen atom H1A. The observed charge distribution shifts are typical for hydrogen bond formation. The topological analysis of the electron density for linear conformation (computed on a B3LYP/6-311++G(d,p) level of theory) shows the bond critical point ($\rho_{BCP} = 0.0201$; $\nabla^2\rho_{BCP} = 0.0933$) and corresponding ring critical point ($\rho_{RCP} = 0.0201$; $\nabla^2\rho_{RCP} = 0.1039$) of the intramolecular hydrogen bond (Fig. S5 in Online Resources). However, when the dispersion correction was applied, the electron density was not sufficient to determine the bond or the ring critical points for this interaction.

Conclusions

1. The monocrystals of two forms of the carbamohydrazoneothioate derivative were successfully obtained. The crystal structure solution and refinement revealed that the one is the pure component (CHT) and the other is the hydrochloride solvate (CHT-salt). The main difference for the CHT molecule within crystal structures is conformation.
2. The bent conformation of the ligand molecule allows to form the two types of the cyclic hydrogen bonds within the CHT crystal structure. The N–H \cdots N and C–H \cdots π -type HBs are alternately arranged; thus, the main motif is easy to spot. In the case of the CHT-salt crystal structure, it is impossible to distinguish main motif. The structure is held together by the net of charge-assisted HBs where the methanol molecule and the chloride ion play the role of the molecular glue.
3. The Hirshfeld surface analysis show that the H \cdots H non-covalent interaction is dominant. It covers about 46% of all

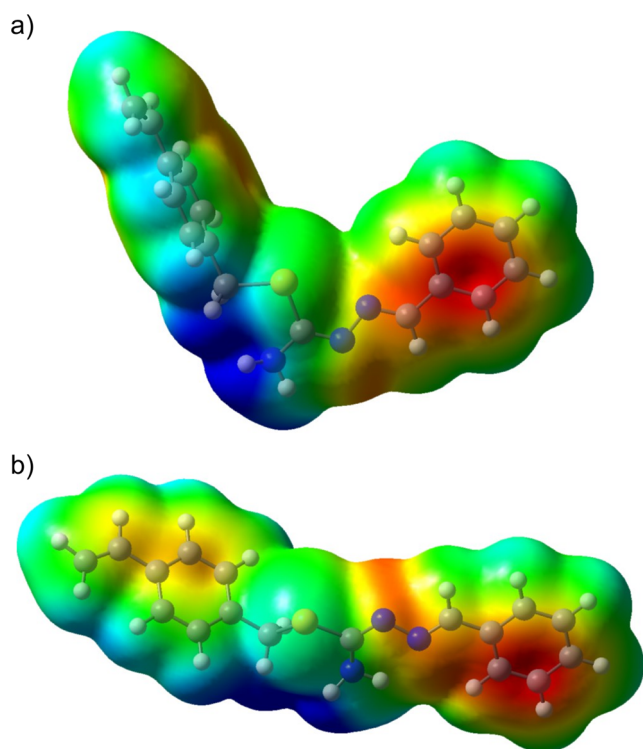


Fig. 10 Electrostatic potentials mapped on the 0.0004 a.u. molecular isosurface of the electron density **a** bent and **b** linear conformations of CHT. The colored scale corresponds to values in range from -0.07 (red) to $+0.007$ (blue) [Hartree]

interactions within the CHT crystal structure and about 50% interactions for the ligand cation within the CHT-salt crystal structure.

- The calculations performed for the dimers of the bent CHT molecule illustrate the importance of application of the dispersion energy corrections. The correct reproduction of the dimers' geometries in relation to the corresponding molecular fragments of the crystal structures shows marginal influence of the crystal packing on the N–H...N and C–H... π dimer formations.
- The possibility of conformational change for CHT molecule was proven with the DFT calculation. The simulation of the rotation process shows that for the isolated molecule, the bent and the linear conformation energies are equal. The rotation barrier is high (around 96 kJ (23 kcal/mol)); thus, the change of the conformation might not be spontaneous.
- The analyses of molecular electrostatic potential explained why the linear conformation of the ligand cannot generate periodic structure. The inconvenient distribution of charges prevents formation of strong non-covalent intermolecular interactions.
- The charge distribution calculated in terms of the QTAIM shows that the change of the conformation does not influence atomic charge population in general. The exception is the hydrazoneformamide fragment where the formation of the intramolecular hydrogen bond occurs.

Acknowledgements This work was financially supported by the National Science Centre, Poland, grant no. NCN/2014/13/N/ST5/01563. The equipment in the Center of Synthesis and Analysis BioNanoTechno of University of Białystok was funded by EU, project no POPW.01.03.00-20-004/11. The calculations using GAUSSIAN 09 were carried out in the Wrocław Centre for Networking and Supercomputing and the Computer Center of University of Białystok.

Open Access This article is distributed under the terms of the Creative Commons Attribution 4.0 International License (<http://creativecommons.org/licenses/by/4.0/>), which permits unrestricted use, distribution, and reproduction in any medium, provided you give appropriate credit to the original author(s) and the source, provide a link to the Creative Commons license, and indicate if changes were made.

References

- Marzano C, Pellei M, Tisato F, Santini C (2009) Copper complexes as anticancer agents. *Anti Cancer Agents Med Chem* 9(2):185–211
- Paterson BM, Donnelly PS (2011) Copper complexes of bis(thiosemicarbazones): from chemotherapeutics to diagnostic and therapeutic radiopharmaceuticals. *Chem Soc Rev* 40(5):3005–3018. doi:10.1039/c0cs00215a
- Pelosi G (2010) Thiosemicarbazone metal complexes: from structure to activity. *The Open Crystallography Journal* 3:16–28
- Casas JS, Garcia-Tasende MS, Sordo J (2000) Main group metal complexes of semicarbazones and thiosemicarbazones. A structural review. *Coord Chem Rev* 209:197–261. doi:10.1016/S0010-8545(00)00363-5
- Lobana TS, Sharma R, Bawa G, Khanna S (2009) Bonding and structure trends of thiosemicarbazone derivatives of metals—an overview. *Coord Chem Rev* 253(7–8):977–1055. doi:10.1016/j.ccr.2008.07.004
- Datta S, Seth DK, Gangopadhyay S, Karmakar P, Bhattacharya S (2012) Nickel complexes of some thiosemicarbazones: synthesis, structure, catalytic properties and cytotoxicity studies. *Inorg Chim Acta* 392:118–130. doi:10.1016/j.ica.2012.05.034
- Dutta S, Basuli F, Castineiras A, Peng SM, Lee GH, Bhattacharya S (2008) Variable coordination modes of benzaldehyde thiosemicarbazones—synthesis, structure, and electrochemical properties of some ruthenium complexes. *Eur J Inorg Chem* 29:4538–4546. doi:10.1002/ejic.200800547
- Kovala-Demertzi D, Yadav PN, Dernertzi MA, Jasiski JP, Andreadaki FJ, Kostas ID (2004) First use of a palladium complex with a thiosemicarbazone ligand as catalyst precursor for the Heck reaction. *Tetrahedron Lett* 45(14):2923–2926. doi:10.1016/j.tetlet.2004.02.062
- Kurt Y, Deniz NG (2015) Iron(III), nickel(II) and zinc(II) complexes based on acetophenone-S-methyl-thiosemicarbazone: synthesis, characterization, thermogravimetry, and a structural study. *J Coord Chem* 68(22):4070–4081. doi:10.1080/00958972.2015.1086760
- Paul P, Butcher RJ, Bhattacharya S (2015) Palladium complexes of 2-formylpyridine thiosemicarbazone and two related ligands: synthesis, structure and, spectral and catalytic properties. *Inorg Chim Acta* 425:67–75
- Prabhu RN, Ramesh R (2012) Catalytic application of dinuclear palladium(II) bis(thiosemicarbazone) complex in the Mizoroki-Heck reaction. *Tetrahedron Lett* 53(44):5961–5965
- Raja N, Ramesh R (2010) Mononuclear ruthenium(III) complexes containing chelating thiosemicarbazones: synthesis, characterization and catalytic property. *Spectrochim Acta A Mol Biomol Spectrosc* 75(2):713–718. doi:10.1016/j.saa.2009.11.044
- Lim JK, Mathias CJ, Green MA (1997) Mixed bis(thiosemicarbazone) ligands for the preparation of copper radiopharmaceuticals: synthesis and evaluation of tetradentate ligands containing two dissimilar thiosemicarbazone functions. *J Med Chem* 40(1):132–136. doi:10.1021/jm9605703
- Buncic G, Donnelly PS, Paterson BM, White JM, Zimmermann M, Xiao Z, Wedd AG (2010) A water-soluble bis(thiosemicarbazone) ligand. A sensitive probe and metal buffer for zinc. *Inorg Chem* 49(7):3071–3073. doi:10.1021/ic902370a
- Kate AN, Kumbhar AA, Khan AA, Joshi PV, Puranik VG (2014) Monitoring cellular uptake and cytotoxicity of copper(II) complex using a fluorescent anthracene thiosemicarbazone ligand. *Bioconjug Chem* 25(1):102–114. doi:10.1021/bc400385d
- Dilworth JR, Huetting R (2012) Metal complexes of thiosemicarbazones for imaging and therapy. *Inorg Chim Acta* 389:3–15. doi:10.1016/j.ica.2012.02.019
- Jansson PJ, Kalinowski DS, Lane DJR, Kovacevic Z, Seebacher NA, Fouani L, Sahni S, Merlot AM, Richardson DR (2015) The renaissance of polypharmacology in the development of anti-cancer therapeutics: inhibition of the “triad of death” in cancer by di-2-pyridylketone thiosemicarbazones. *Pharmacol Res* 100:255–260. doi:10.1016/j.phrs.2015.08.013
- Vandresen F, Falziroli H, Batista SAA, da Silva-Giardini APB, de Oliveira DN, Catharino RR, Ruiz ALTG, de Carvalho JE, Foglio MA, da Silva CC (2014) Novel R-(+)-limonene-based thiosemicarbazones and their antitumor activity against human tumor cell lines. *Eur J Med Chem* 79:110–116. doi:10.1016/j.ejmech.2014.03.086
- Sankaraperumal A, Karthikeyan J, Shetty AN, Lakshmisundaram R (2013) Nickel(II) complex of p-[N,N-bis(2-chloroethyl)amino]benzaldehyde-4-methylthiosemicarbazone: synthesis,

- structural characterization and biological application. *Polyhedron* 50(1): 264–269. doi:[10.1016/j.poly.2012.11.006](https://doi.org/10.1016/j.poly.2012.11.006)
20. Bharti SN, Naqvi F, Azam A (2003) Synthesis, spectral studies and screening for amoebicidal activity of new palladium(II) complexes derived from thiophene-2-carboxaldehyde thiosemicarbazones. *Bioorg Med Chem Lett* 13(4):689–692
 21. Soykan C, Erol I (2003) Synthesis, characterization, and biological activity of N-(4-acetylphenyl)maleimide and its oxime, carbazone, thiosemicarbazone derivatives and their polymers. *J Polym Sci Pol Chem* 41(13):1942–1951. doi:[10.1002/pola.10738](https://doi.org/10.1002/pola.10738)
 22. Genova P, Varadinova T, Matesanz AI, Marinova D, Souza P (2004) Toxic effects of bis(thiosemicarbazone) compounds and its palladium(II) complexes on herpes simplex virus growth. *Toxicol Appl Pharm* 197(2):107–112. doi:[10.1016/j.taap.2004.02.006](https://doi.org/10.1016/j.taap.2004.02.006)
 23. Garg BS, Jain VK (1988) Analytical applications of thiosemicarbazones and semicarbazones. *Microchem J* 38(2): 144–169. doi:[10.1016/0026-265x\(88\)90017-3](https://doi.org/10.1016/0026-265x(88)90017-3)
 24. Ashok Kumar SL, Saravana Kumar M, Sreeja PB, Sreekanth A (2013) Novel heterocyclic thiosemicarbazones derivatives as colorimetric and “turn on” fluorescent sensors for fluoride anion sensing employing hydrogen bonding. *Spectrochim Acta A Mol Biomol Spectrosc* 113:123–129. doi:[10.1016/j.saa.2013.04.103](https://doi.org/10.1016/j.saa.2013.04.103)
 25. Udhayakumari D, Suganya S, Velmathi S (2013) Thiosemicarbazone based fluorescent chemosensor for transition metal ions in aqueous medium. *J Lumin* 141:48–52. doi:[10.1016/j.jlumin.2013.03.023](https://doi.org/10.1016/j.jlumin.2013.03.023)
 26. Suganya S, Udhayakumari D, Velmathi S (2013) Heterocyclic thiosemicarbazones as fluorescent sensors for the selective recognition of cations in the aqueous phase. *Anal Methods-Uk* 5(16): 4179–4183. doi:[10.1039/c3ay40381e](https://doi.org/10.1039/c3ay40381e)
 27. Markiewicz KH, Zembko P, Poltorak K, Misztalewska I, Wojtulewski S, Majcher AM, Fornal E, Wilczewska AZ (2016) Magnetic nanoparticles with chelating shells prepared by RAFT/MADIX polymerization. *New J Chem*. doi:[10.1039/C6NJ01938B](https://doi.org/10.1039/C6NJ01938B)
 28. Li C, Meng LZ, Lu XJ, Wu ZQ, Zhang LF, He YB (2005) Thermo- and pH-sensitivities of thiosemicarbazone-incorporated, fluorescent and amphiphilic poly(N-isopropylacrylamide). *Macromol Chem Phys* 206(18):1870–1877. doi:[10.1002/macp.200500222](https://doi.org/10.1002/macp.200500222)
 29. Lu XJ, Gong SL, Meng LZ, Li C, Liang F, Wu ZQ, Zhang LF (2007) Novel fluorescent amphiphilic block copolymers: controllable morphologies and size by self-assembly. *Eur Polym J* 43(7): 2891–2900. doi:[10.1016/j.eurpolymj.2007.04.006](https://doi.org/10.1016/j.eurpolymj.2007.04.006)
 30. Diffraction RO Rigaku Oxford Diffraction (2014) CrysAlisPro software system, version 1.171.37.35. Rigaku Corporation, Oxford
 31. Sheldrick GM (2008) A short history of SHELX. *Acta Crystallogr A* 64:112–122. doi:[10.1107/S0108767307043930](https://doi.org/10.1107/S0108767307043930)
 32. Bourhis LJ, Dolomanov OV, Gildea RJ, Howard JAK, Puschmann H (2015) The anatomy of a comprehensive constrained, restrained refinement program for the modern computing environment—OLEX2 dissected. *Acta Crystallogr A* 71(1):59–75. doi:[10.1107/S2053273314022207](https://doi.org/10.1107/S2053273314022207)
 33. Dolomanov OV, Bourhis LJ, Gildea RJ, Howard JAK, Puschmann H (2009) OLEX2: a complete structure solution, refinement and analysis program. *J Appl Crystallogr* 42(2):339–341. doi:[10.1107/S0021889808042726](https://doi.org/10.1107/S0021889808042726)
 34. Spackman MA, Jayatilaka D (2009) Hirshfeld surface analysis. *CrystEngComm* 11(1):19–32. doi:[10.1039/b818330a](https://doi.org/10.1039/b818330a)
 35. Spackman MA, McKinnon JJ, Jayatilaka D (2008) Electrostatic potentials mapped on Hirshfeld surfaces provide direct insight into intermolecular interactions in crystals. *CrystEngComm* 10(4):377–388. doi:[10.1039/b715227b](https://doi.org/10.1039/b715227b)
 36. Becke AD (1993) Density-functional thermochemistry .3. The role of exact exchange. *J Chem Phys* 98(7):5648–5652
 37. Lee CT, Yang WT, Parr RG (1988) Development of the Colle-Salvetti correlation-energy formula into a functional of the electron-density. *Phys Rev B* 37(2):785–789. doi:[10.1103/PhysRevB.37.785](https://doi.org/10.1103/PhysRevB.37.785)
 38. Stephens PJ, Devlin FJ, Chabalowski CF, Frisch MJ (1994) Ab-initio calculation of vibrational absorption and circular-dichroism spectra using density-functional force-fields. *J Phys Chem-US* 98(45):11623–11627. doi:[10.1021/J100096a001](https://doi.org/10.1021/J100096a001)
 39. Miehlich B, Savin A, Stoll H, Preuss H (1989) Results obtained with the correlation-energy density functionals of Becke and Lee, Yang and Parr. *Chem Phys Lett* 157(3):200–206. doi:[10.1016/0009-2614\(89\)87234-3](https://doi.org/10.1016/0009-2614(89)87234-3)
 40. Frisch MJ, Trucks GW, Schlegel HB, Scuseria GE, Robb MA, Cheeseman JR, Scalmani G, Barone V, Mennucci B, Petersson GA, Nakatsuji H, Caricato M, Li X, Hratchian HP, Izmaylov AF, Bloino J, Zheng G, Sonnenberg JL, Hada M, Ehara M, Toyota K, Fukuda R, Hasegawa J, Ishida M, Nakajima T, Honda Y, Kitao O, Nakai H, Vreven T, Montgomery Jr JA, Peralta JE, Ogliaro F, Bearpark MJ, Heyd J, Brothers EN, Kudin KN, Staroverov VN, Kobayashi R, Normand J, Raghavachari K, Rendell AP, Burant JC, Iyengar SS, Tomasi J, Cossi M, Rega N, Millam NJ, Klene M, Knox JE, Cross JB, Bakken V, Adamo C, Jaramillo J, Gomperts R, Stratmann RE, Yazyev O, Austin AJ, Cammi R, Pomelli C, Ochterski JW, Martin RL, Morokuma K, Zakrzewski VG, Voth GA, Salvador P, Dannenberg JJ, Dapprich S, Daniels AD, Farkas Ö, Foresman JB, Ortiz JV, Cioslowski J, Fox DJ (2009) Gaussian 09. Gaussian, Inc., Wallingford
 41. Krishnan R, Binkley JS, Seeger R, Pople JA (1980) Self-consistent molecular-orbital methods .20. Basis set for correlated wave-functions. *J Chem Phys* 72(1):650–654. doi:[10.1063/1.438955](https://doi.org/10.1063/1.438955)
 42. Grimme S (2006) Semiempirical GGA-type density functional constructed with a long-range dispersion correction. *J Comput Chem* 27(15):1787–1799. doi:[10.1002/jcc.20495](https://doi.org/10.1002/jcc.20495)
 43. Wang NX, Wilson AK (2004) The behavior of density functionals with respect to basis set. I The correlation consistent basis sets *Journal of Chemical Physics* 121(16):7632–7646. doi:[10.1063/1.1792071](https://doi.org/10.1063/1.1792071)
 44. Curtiss LA, Raghavachari K, Redfern PC, Pople JA (2000) Assessment of Gaussian-3 and density functional theories for a larger experimental test set. *J Chem Phys* 112(17):7374–7383. doi:[10.1063/1.481336](https://doi.org/10.1063/1.481336)
 45. Cohen AJ, Mori-Sanchez P, Yang WT (2012) Challenges for density functional theory. *Chem Rev* 112(1):289–320. doi:[10.1021/cr200107z](https://doi.org/10.1021/cr200107z)
 46. Sousa SF, Fernandes PA, Ramos MJ (2007) General performance of density functionals. *J Phys Chem A* 111(42):10439–10452. doi:[10.1021/jp0734474](https://doi.org/10.1021/jp0734474)
 47. Young DC (2001) Computational chemistry: a practical guide for applying techniques to real world problems. Wiley, New York
 48. Boys SF, Bernardi F (1970) Calculation of small molecular interactions by differences of separate total energies—some procedures with succed errors. *Mol Phys* 19(4):553–566. doi:[10.1080/00268977000101561](https://doi.org/10.1080/00268977000101561)
 49. Bader RFW (1990) Atoms in molecules: a quantum theory. The international series of monographs on chemistry, vol 22. Clarendon Press, Oxford
 50. Popelier PLA (2000) Atoms in molecules: an introduction. Prentice Hall, Harlow
 51. Software TAKTG (2015) AIMAll (Version 15.08.29), Todd A. Keith, TK Gristmill Software, Overland Park KS, USA, 2015 (aim.tkgristmill.com)
 52. Desiraju GR, Steiner T (1999) The weak hydrogen bond in structural chemistry and biology. International Union of Crystallography book series IUCr monographs on crystallography, vol 9. Oxford University Press, Oxford
 53. Grabowski SJ (2009) Covalent character of hydrogen bonds enhanced by pi-electron delocalization. *Croat Chem Acta* 82(1):185–192
 54. Philp D, Robinson JMA (1998) A computational investigation of cooperativity in weakly hydrogen-bonded assemblies. *J Chem Soc Perk T* 2(7):1643–1650. doi:[10.1039/A800931g](https://doi.org/10.1039/A800931g)